Hydroxyapatite reinforced Ti6Al4V composites for load-bearing implants

Jose D. Avila, Kevin Stenberg, Susmita Bose, and Amit Bandyopadhyay*

W. M. Keck Biomedical Materials Research Lab

School of Mechanical and Materials Engineering

Washington State University, Pullman, WA 99164, USA

†Corresponding author e-mail: amitband@wsu.edu

Abstract

Titanium has been used in various biomedical applications; however, titanium exhibits poor wear resistance, and its bioinert surface slows osseointegration *in vivo*. In this study, directed energy deposition (DED)-based additive manufacturing (AM) was used to process hydroxyapatite (HA) reinforced Ti6Al4V (Ti64) composites to improve biocompatibility and wear resistance simultaneously. Electron micrographs of the composites revealed dense microstructures where HA is observed at the β-phase grain boundaries. Hardness was observed to increase by 57% and 71% for 2 and 3 wt.% HA in Ti64 composites, respectively. XRD analysis revealed no change in the present phases. Tribological studies revealed an increase in contact resistance due to *in situ* HA-based tribofilm formation, reduction in wear rate when testing in DMEM with a ZrO_2 counter wear ball, <1% wear ball volume loss, and suppression of cohesive failure of the Ti matrix. Histomorphometric analysis from a rat distal femur study revealed an increase in the osteoid surface over the bone surface (OS/BS) for 3 wt.% HA composite over the control Ti64 from 9 ± 1% to 14 ± 1%. Shear modulus was also observed to increase from 17 ± 3 MPa for control Ti64 to 32 ± 5 MPa for the 3 wt.% HA composite after 5 weeks. Our study demonstrates that the addition of HA in Ti64 can simultaneously improve bone tissue-implant response and wear resistance.

Keywords: Hydroxyapatite; Ti6Al4V; Additive manufacturing; Directed energy deposition; Wear resistance.

1.0 Introduction

Bone disorder is increasing steadily worldwide due to the aging population, more active lifestyle, and deteriorating food habits [1]. Although many treatment options for bone disorders have matured and improved the quality of life for patients in need, there are still unmet needs in the area of load-bearing implants. For load-bearing implants, titanium (Ti) and its alloys are common due to Ti's excellent corrosion and fatigue resistance along with cytocompatibility. However, Ti exhibits poor wear resistance and is not suitable for articulating surfaces [2]. Current material options for articulating surfaces include CoCr alloys or all-ceramic devices. Concerns related to Co^{2+} and Cr^{3+} ions leaching from CoCr alloys due to bio-tribo-corrosion exist; Co^{2+} and Cr^{3+} ions in the body further cause adverse local tissue reactions (ALTR) [3], which result in implant failure and require early revision surgery [4,5]. As an alternative to CoCr alloys, alumina-based ceramics are becoming popular, particularly with younger patients [6]. In a recent study, out of 345 patients with ceramic-on-ceramic devices at their 5.3-year follow-up, 1% reported fracture, 3% already had revision surgery, and 7.5% reported a squeaking sound coming from their implant [7]. Simply put, very little longer-term data is available today for ceramic-based implants to prove that it is an excellent viable alternative, while concerns still exist based on published data.

Many techniques to increase the bioactivity of Ti and its alloys have been reported. Calcium phosphate (CaP) coatings deposited by plasma-spray methods have shown significant bioactivity improvements and are commonly used in load-bearing implants, particularly for

patients needing revision surgery [8]. However, processes such as plasma-spray require direct line-of-sight. Line-of-sight techniques are limited to applications involving simple geometry and near-orthogonal surfaces. Similar to improving Ti alloys' biocompatibility, several attempts have also been reported for improving wear resistance. Ti surfaces have been coated with hard ceramic materials to improve wear resistance. Such ceramic coatings have been done using chemical vapor deposition (CVD) or physical vapor deposition (PVD) [9,10], ion and plasma beam treatment [11,12], gas nitriding, and laser-based nitriding [13,14]. However, a sharp and incoherent interface between the metal and the ceramic phases causes the coatings' poor mechanical performance *in vivo*.

The objective of this research is to simultaneously increase wear resistance and biocompatibility of Ti64 alloy by the addition of HA. The central hypothesis to improve wear resistance is that HA will allow for the formation of an *in situ* tribofilm on the contact surface during articulation. If formed, the *in situ* tribo-film will minimize the direct contact between the two surfaces in relative motion and minimize wear induced damage; similar to what the body naturally does via cartilage and synovial fluid in human joints. For every joint in our body, direct contact between two hard cortical bone surfaces is avoided by a soft cartilage layer, allowing for the reduction of the coefficient of friction (COF) and wear induced damage. Our biomimetic concept to use a soft tribofilm is to replicate cartilage-like behavior in an acellular material to minimize COF and wear induced damage. Considering HA has been reported to improve upon tissue response, the addition of HA in Ti64 should also improve the composites' biocompatibility, resulting in improved early-stage osseointegration. Therefore, it is envisioned that the addition of HA in Ti64 will simultaneously initiate tribofilm formation for improved wear resistance and enhance biocompatibility. In this study, structures of Ti64, Ti64 reinforced

with 2 wt.% HA and 3 wt.% HA were processed using directed energy deposition (DED)-based additive manufacturing (AM). Microstructure and phase analysis of samples were done by scanning electron microscopy (SEM) and x-ray diffraction (XRD), respectively. Vickers micro-hardness measurements were done for surface mechanical properties. The samples' wear performance was measured using bio-tribological testing under a fully immersed condition in deionized (DI) water and DMEM cell media using tungsten carbide, hardened chrome steel, and zirconia balls. Finally, the biocompatibility was measured using a rat distal femur bi-lateral *in vivo* model followed by histological analysis.

2.0 Materials and methods

Sample fabrication: Samples were fabricated using a DED-based AM technique, laser-engineered net shaping (LENS™-750, Optomec, NM). Our LENS™ system is equipped with a 500W continuous-wave Nd:YAG laser. Samples were fabricated in an argon environment, with an oxygen concentration of <20ppm. Powders used were Ti64 (TEKNA. Canada; Grade 23, -100/+325 mesh) with an average particle size of 45 – 150µm, and HA powder (Berkeley Advanced Biomaterials, Inc., CA, USA) with particle size <500nm. Feedstock powders were of pure Ti64, Ti64 + 2 wt.% HA (2HA) and Ti64 + 3 wt.% HA (3HA). Composite powders 2HA and 3HA were ball-milled for 6 – 8h with 10mm diameter alumina milling balls in sealed argon containers. Powder-to-milling ball ratio was roughly 2:1 and milled between 20 – 30 rpm. Tribological samples were fabricated on 3mm thick Grade 5 Ti64 substrate (President Titanium, Hanson, MA, USA), having a geometry of 14mm x 18mm rectangles with an average height of 3mm. Additionally, these samples were used for hardness, microstructure, and phase analysis. Cylindrical samples for the *in vivo* rat distal femur model were first fabricated with a nominal

diameter of 5mm, and then mechanically turned down to 3mm diameter, sectioned at the height of 5mm, and then implanted. Processing parameters of the LENS™ system for fabrication of Ti64, 2HA, and 3 HA samples are shown in **Table 1**.

Microstructural characterization and phase analysis: DED produced samples were ground up to 2000 grit using SiC grinding paper followed by polishing to a mirror finish using 1.0, 0.3, and 0.05μm alumina powders suspended in DI water. The etching was performed by Kroll's Reagent (92ml DI water, 6ml nitric acid, 2ml hydrofluoric acid) by fully submerging the samples for 15s. Scanning electron microscopy (SEM) was done using a field-emission scanning electron microscope (FESEM, FEI-SIRION, Portland, OR) with EDAX attachment for EDS analysis. The average grain size was reported from electron micrograph images using the average grain intercept (AGI) method. Six randomly oriented lines per image were used to estimate the average grain size of each composition. X-ray diffraction data for phase analysis was attained using a PANalytical X'pert Pro MPD XRD machine using Cu-Kα radiation (1.54 Å), scanning from 20 to 80 2θ degrees at a step size of 0.05 2θ degrees with a 6s dwell time. Phase identification was made using reference cards from the International Centre for Diffraction Data (ICDD) and the Joint Committee on Powder Diffraction Standards (JCPDS). Reference cards used for phase analysis of Ti64, 2HA, and 3HA samples were ICDD:98-004-3416 (α-Ti), ICDD:98-015-1409 (β-Ti), and JCPDS#: 09-0432 (HA, $Ca_5(PO_4)_3(OH)$). The EDS analysis of the microstructure was performed for phosphorus mapping.

Hardness and wear characterization: Surface microhardness was measured using a Phase II Plus, Micro Vickers hardness tester (Upper Saddle River, NJ, USA) with a 200g load and 15s

dwell time. Several tribological tests were performed to explore the produced samples' wear behaviors where the counter wear ball and the media were varied. The counter wear balls used were of tungsten carbide (WC), hardened chrome steel (HCS), and zirconium dioxide (ZrO_2), while the media varied from DI water to Dulbecco's Modified Eagle Medium (DMEM). Testing of WC was conducted on a fully automated tribometer (Nanovea, Irvine CA, USA), while testing of HCS and ZrO_2 was conducted on a single station Biotribometer (Ducom, India). The Ducom Biotribomter uses a 2-wire circuit with a known current to measure the contact resistance (CR) during tribological testing; therefore, electrically conductive wear balls were used for these tests. Testing was conducted as per ASTM G133-05, the standard test method for linearly reciprocating ball-on-flat sliding wear [15]. Tribological testing was done with a normal load of 7N, in DI water and DMEM, at room temperature for a total sliding distance of 1000m at a linear velocity of 1200mm·min^{-1} with a 10mm stroke length. Post-tribological electron micrographs of the wear tracks were used to calculate the wear rate; this was done by measuring the wear track width first and then calculating the wear track *trough* cross-section, followed by trough volume calculated by multiplication with the stroke, and finally normalizing by the product of the applied load and total slide distance; as per the standard [15]. Visual aid may be observed online at the following source [16]. Equations used were as follows:

$$\theta_w = 2 \arcsin\left(\frac{w}{2r}\right)$$

$$V_w = A_w * l = \frac{r^2}{2}(\theta_w - \sin(\theta_w)) * l$$

$$Normalized\ Wear\ Rate = \frac{V_w}{F_N * S}$$

Where w is the wear track width (mm), r is the radius of the worn ball (mm), θ_w is the included adjacent angle of the produced isosceles triangle with base length w and side lengths r,

A_w is the cross-sectional area of the wear track (mm^2), l is the stroke length (mm), V_w is the wear track volume (mm^3), F_N is the applied normal load in (N) and S is the total slide distance (m). Additionally, the wear scar on the counter wear ball was imaged to determine the final contact pressure and volume loss; and measured values are listed in **Table 2**. EDS elemental mappings of the wear scar were also attained to further understand the wear system and identify material transfer.

In vivo rat study: 12 male Sprague-Dawley rats weighing roughly 300g were used for *in vivo* studies. Bilateral surgery at the distal femur was done. Before surgery, *in vivo* test protocols were approved by the Institutional Animal Care and Use Committee (IACUC) at Washington State University (WSU, Pullman, WA). Rats were housed in pairs with 12h cycling of light and darkness. Before surgery, rats were anesthetized with IsoFlo® (isoflurane, USP, Abbott Laboratories, North Chicago, IL, USA) coupled with oxygen (Oxygen USP, A-L Compressed Gases Inc., Spokane, WA, USA). The monitoring of anesthetic effects was done by pedal reflex and rate of respiration. Before incision, hair was removed to expose the surgery site, which was then disinfected using alternating isopropyl alcohol and chlorhexidine in triplicates. A cylindrical defect was created in the distal femur using sterilized stainless-steel drill bits, increasing diameter up to 3mm. Before the implantation of samples, rinsing of the defect was done with saline solution. Once implantation was performed, fascia tissue was sutured using resorbable sutures (coated MONOCRYL-polyglactin 910, Ethicon Inc., Somerville, NJ, USA). The incision was topically closed using surgical staples. Betadine solution was used to sanitize the incision, and 3ml of saline was administered subcutaneously for hydration. Post-surgery anti-inflammatory analgesic meloxicam was administered in the form of a subcutaneous injection.

Floor feeding of water-softened feed was done during the monitoring period. Single rat housing was done post-surgery, and environmental stimuli were present in soft bedding (paper shreds) and housing tube. After 5 and 12 weeks, rats were euthanized by overdosing of carbon dioxide until the heartbeat was undetectable and then maintained in the chamber one full minute after the termination of gas delivery. An auxiliary method for death confirmation was also performed (pneumothorax). Surgery and euthanasia were performed following the set protocol approved by the IACUC of WSU.

Histological analysis and push-out testing: Harvested femurs were preserved in 10% buffered formalin solution. Radiographic exposures were attained with IVIS® Spectrum CT using an X-ray energy source and evaluated using computed tomography (CT). Scanning of the femurs was done at 40µm voxel size and 150µm pixel size. Three-dimensional images were constructed using Living Image® Software. Dehydration was carried out in increasing ethanol concentrations and acetone; 70, 95, and 100% ethanol followed by 1:1 acetone-ethanol and finally 100% acetone. Femurs were allowed to idle in each solution for 24h. Once dehydrated, femurs were embedded in Spurrs resin and then sectioned into thin slices. Masson Goldner's trichrome staining method was performed for osteoid and bone mineralization determination, and optical photomicrographs were collected with an optical light microscope (Olympus BH-2, Olympus America Inc., USA). Histomorphometric analysis was done as per the published standard [17–20]. Osteoid colors, red/orange, were isolated from other spectrum colors, and surface area percent was calculated within the region of interest (ROI); ROI bandwidth was set to 0.75mm. Osteoid percentage represented the osteoid surface over the bone surface (OS/BS) and was determined by the use of Gimp 2.8 software. Push-out testing was done to quantify

interfacial bond strength between the host tissue and the implant. Testing was done using a uniaxial press (Instron, PA, USA) in compression with a 22.7kg load cell. The depth of the implant in the femur was measured to determine the surface area of interaction. Stress-strain plots were acquired to measure the interfacial shear modulus from the linear slope of the plots.

Statistical Analysis: Statistical analysis was conducted for hardness and OS/BS data. To maintain the $\alpha = 0.05$ significance, a single factor ANOVA test was first performed across all the compositions' averages. After that, pair-wise student t-testing was done if the ANOVA results determined a difference in means.

3.0 Results

HA reinforced Ti64 composite samples were fabricated from premixed feedstock powders by DED-based AM. Hardness, microstructure, phase analysis, tribological, and *in vivo* studies were conducted to understand the influence of HA reinforcement on Ti64 towards wear resistance and tissue-materials interactions.

Microstructure, phase analysis, and hardness: Electron micrographs of the acid-etched Ti64 composition revealed β-titanium (β-Ti) grain boundaries along with a transformed intragranular acicular α-Ti needle-like grain structure (α'-Ti), **Fig. 1A**. With the addition of HA, intragranular α'-Ti grains were still observed in composites 2HA and 3HA; however, grain refinement was observed for the initially formed β-Ti grains, **Fig. 1B,** and **1C**. Composite 3HA displayed a similar microstructure as 2HA; however, the average grain size decreased. The average grain size of α'-Ti grains for Ti64, 2HA, and 3HA compositions were 35 ± 2, 10 ± 1, and 7 ± 1 μm, respectively. Additionally, the presence of HA was observed at the β-Ti grain boundaries for 2HA and 3HA compositions and was validated by phosphorus mapping, **Fig. 1D**.

Acquired X-ray diffraction (XRD) spectrums for the compositions are presented in **Fig. 2**. Ti64 displayed only the α-Ti phase, while 2HA and 3HA exhibited similar spectra as Ti64. The intensity peak at 2θ = 39.4 degrees represents the (310) diffraction planes of HA and is the most predominant for 3HA. Additionally, it appears to be the minimum weight percent for detection as the HA peak is not observed in the 2HA composition. Vickers hardness values for all compositions are displayed in **Fig. 3**. The measured hardness for Ti64 was 377 ± 21 $HV_{0.2}$, whereas composites 2HA and 3HA displayed an increase in hardness to 592 ± 25 $HV_{0.2}$ and 645 ± 33 $HV_{0.2}$, respectively. Compared to Ti64, 2HA and 3HA displayed a 57% and 71% increase in hardness, respectively.

Tribological studies: Compound wear (CW), normalized wear rate, coefficient of friction (COF), and contact resistance (CR) data are displayed in **Fig. 4** for the Ti64, 2HA, and 3HA compositions. In DI water and with a WC counter wear ball, 3HA exhibited the most significant compound wear with Ti64 and 2HA displaying relatively similar CW throughout testing. Grouping the CW for the three compositions was observed when testing in DI water with an HCS counter wear ball, with 3HA continued to exhibit a slightly higher CW magnitude as testing progressed. When testing in DMEM with a ZrO_2 counter wear ball – the most biomedical applicable scenario – Ti64 exhibited the greatest CW at ~200µm with 2HA and 3HA remaining under 60µm. By the CW curve, 3HA appeared to have material adhere on the surface as a reduction in CW was observed at ~700m; similarly, this was observed for 2HA at ~900m. The normalized wear rate for Ti64 was the lowest when testing in DI water with a WC counter wear ball. 3HA exhibited the highest overall normalized wear rate and only reducing to values lower than Ti64 and 2HA after ~800m of tribological testing. When testing in DI with an HCS counter

wear ball, the normalized wear rates deviate less amongst the three compositions, with 2HA exhibiting the most significant fluctuation and Ti64 displaying the least. Testing in DMEM with a ZrO_2 counter wear ball resulted in both 2HA and 3HA displaying lower normalized wear rates than Ti64. Negative normalized wear rate values are associated with material adhering to the wear surface. COF across all combinations of media and counter wear ball was generally the lowest for Ti64. The 2HA composition emulated the observed COF of Ti64 in DI water with a WC counter wear ball after overcoming the running-in wear regime and upon steady-state wear. Both compositions, 2HA and 3HA exhibiting similar COF in DI water and DMEM when testing with an HCS or ZrO_2 wear ball, respectively. Additionally, CR was monitored and logged during tribological testing. For most tribological testing, Ti64 remained at lower CR values when compared to 2HA and 3HA. A small deviation to ~40 Ω was observed from ~500 – 700m when testing in DI water with a WC counter wear ball but subsided before the end of testing. CR for 2HA remained around ~40Ω for the entirety of the test, while 3HA progressively increased to ~ 160Ω at ~800m, with 3 observed fluctuations due to the formation and removal of a tribofilm. When testing in DI water with an HCS wear ball, all compositions displayed less fluctuation, with 2HA and 3HA continually exhibiting higher CR values.

To further understand the tribological characteristics associated with each composition, surface imaging of the wear scars was done and are displayed in **Fig. 5**. The Ti64 surface morphology across all three testing conditions was similar; that is, observed on the surface was mechanically adhered debris and formation of fractures along the grooves, and the results of severe plastic deformation. Suppression of this aggressive wear behavior was observed with HA's presence, with the best results arising when testing in DMEM with a ZrO_2 counter wear ball for the 3HA composition. Grooving, plowing, and plastic deformation of the Ti-based matrix

was not observed; instead, a smooth wear track was apparent. Wear involves the relative motion and interaction of two materials; therefore, the counter wear balls were also imaged and are displayed in **Fig. 6**. Wear scars were measured for wear ball volume loss and final contact pressure calculation, as listed in **Table 2**.

Additionally, Ti EDS elemental maps of the HCS wear ball were attained and are displayed in **Fig. 7**. All counter wear balls exhibited <1% volume loss across all testing conditions. While testing in DI water with a WC counter wear ball, the 3HA tested WC wear ball accounted for the most significant wear at 0.92% but reduced to 0.04% when tested with the 2HA composition. In DI water with an HCS counter wear ball tested with the Ti64 composition, the HCS wear ball showed the most significant volume loss at 0.30%, and when tested with the 2HA composition, it exhibited the lowest at 0.06%. In DMEM and with a ZrO_2 counter wear ball tested with the Ti64 composition, the ZrO_2 wear ball displayed the most significant volume loss at 0.76%, and when tested with the 2HA composition, the ZrO_2 wear ball displayed the least volume loss at 0.30%. Therefore, across all tribological testing conditions, the 2HA composition allowed for the least amount of wear on the counter material. Observed in the Ti64/ZrO_2/DMEM tribological system was the cohesive failure of the Ti64 sample and invoked the most adhesive wear, visible by the amount of material transfer present on the worn ball. The 3HA/ZrO_2/DMEM tribological system displayed the least. Cohesive failure of the Ti matrix is also observed for the Ti64/HCS/DI tribological system. The Ti elemental mapping, shown in **Fig. 7**, for HCS displays the results of adhesive wear as Ti is observed on the HCS wear ball surface. This is also true for 2HA and 3HA when tested in DI water with HCS but adhered Ti is reduced. When examining the 3HA/WC/DI tribological system, Ti debris is also visible on the WC counter wear ball. Additionally, contact pressure varies the least amongst the three compositions when testing in

DMEM with a ZrO_2 counter wear ball and the most in DI water with a WC wear ball. To further understand the improvements most observed in the 3HA/ZrO_2/DMEM tribological system, EDS analysis was conducted, and a phosphorus elemental map was acquired, **Fig.8**. It would appear that HA is present on the wear track surface and filmed the surface via HA-based tribofilm.

In vivo study: The *in vivo* specimens were additively manufactured, mechanically turned, sterilized, implanted, harvested, and prepared for histomorphometric analysis, as shown in **Fig. 9**. It is observed from the CT scans that no defects were present, and proper specimen implantation was performed. Once harvested, the femurs were dehydrated, Spurrs resin embedded, sectioned, modified Masson Goldner trichrome stained, and optical images of the harvested femur/implant section were collected for histomorphometric analysis, as shown in **Figs. 10** and **11**. The presence of new bone, osteoid formation, is represented by the red/orange color. In the 5-week harvested femurs, the osteoid presence was observed in the Ti64 control; however, a greater amount was observed in the 2HA implanted specimen, with the highest amount observed in the 3HA specimen. OS/BS for the Ti64, 2HA, and 3HA specimens were 9 ± 1%, 10 ± 1%, and 14 ± 1%, respectively. Similarly, observed in **Fig. 11**, the 12-week images revealed the increased presence of osteoid within the ROI for the Ti64 implanted specimen; however, it was observed that in the 2HA and 3HA implanted specimens, a more uniform distribution of osteoid presence was nurtured; thereby, it would clear that the 2HA and 3HA specimens continually promoted new bone formation up to 12-weeks. Shear modulus values from push-out testing are displayed in **Table 3**, along with reported values for similar studies as a comparison. Although 5-week and 12-week time points were used to investigate the biocompatibility and early-stage osseointegration of the specimens, all 12-week femurs fractured during push-out testing rendering the data useless for interfacial shear modulus determination.

Such femur fractures are common if the host tissue bonds strongly with the implant; only 5-week data is tabulated. Early-stage osseointegration is the focus of the current study, and 5-week data is of greater interest with regards to the calculated shear modulus. The Ti64 specimen's shear modulus was 17 ± 3MPa, while the average shear modulus values for the 2HA and 3HA specimens were 25 ± 2MPa 32 ± 5MPa, respectively. Thereby, it equates to a 47% and 88% increase for the 2HA and 3HA specimens compared to the Ti64 specimen, respectively.

4.0 Discussion

Microstructure, phase analysis, and hardness: SEM micrographs coupled with the XRD results revealed that the Ti64 composition primarily consisted of an α-titanium (α-Ti) phase; the structure is typical and is a result of high cooling rates above the β-transus line of α-β Ti alloys post-directed-energy deposition. Such microstructure has been observed before in AM processed structures and is commonly referred to as α'-Ti; it differs from α-Ti like being supersaturated in β-phase stabilizing elements [21,22]. The fast cooling rates associated with the directed-energy deposition process limit these elements' outward diffusion from the initially formed β-phase upon solidification [23,24]. Therefore, complete phase transformation to α-Ti does not occur, and the resulting phase is referred to as α'-Ti. Data from XRD compliments the SEM images, expressing mainly the α-Ti phase. Based on the reference cards, β-Ti would have the 100% intensity characteristic peak (011) at 2θ = 38.3 degrees, close to the 25.5% intensity (002) peak of α-Ti at 2θ = 38.4 degrees. β-Ti peaks are not seen in the XRD plot in **Fig 2**, although it could be argued that the β-Ti (011) diffraction planes could be present, as a result of convolution, clear discernment is not possible. Peak overlap and the fact that the microstructure is predominately α'-Ti produce weak β-Ti peaks, making the identification and discernment of β-Ti difficult. SEM

micrographs of Ti64 control further verify these results due to the lack of untransformed β-Ti grains. Considerable differences in the corrosion rate between β-Ti and α-Ti, under acidic conditions, exist. Therefore, distinguishing the physical appearance of microstructure would be possible in the SEM micrographs after acid etching. This is because β-Ti is less stable than α-Ti, at room temperature and would, therefore, dissociate at a greater rate producing differences in surface morphology and allowing for the discernment from the α-Ti grains [25]. Considerable difference in the microstructure was not observed in **Fig. 1A**. Observable, apart from the α'-Ti microstructure, were the initially formed β-Ti grain boundaries.

It was observed from the SEM micrographs for the 2HA and 3HA compositions that HA was present at the grain boundaries creating quasi-equiaxed grains, as displayed in the phosphorus elemental mapping of **Fig. 1D**. HA is composed of calcium (Ca^{2+}) and phosphate group (PO_4^{3-}), where phosphorus (P) has been known to be a β-phase stabilizer [26], and oxygen (O) is an α-phase stabilizer for Ti. XRD data revealed α-phase Ti and HA predominantly. Therefore, it can be stated that HA is insoluble or has limited solubility in the Ti64 matrix as it is present at the grain boundaries. A possible explanation for this is that after Ti nucleation and grain growth, HA remains at the solid-liquid interface, i.e., solidification front. Thus, allowing for what appears to be a decrease in grain size with the increased presence of HA. It would seem that upon nucleation, grain growth, and subsequent grain collision, HA remained at the grain boundary and prevented grain growth via Zener pinning; this is apparent when HA content is increased from 2 wt.% to 3 wt.%, the formation of the previously mentioned partially-equiaxed grains become refined; a possible result of increased grain pinning. The average grain size for Ti64 was calculated to be 35 ± 2μm, 2HA was 10 ± 1μm, and 3HA was 7 ± 1μm. A decrease of 68% of the average grain size occurred from the 2HA to 3HA composition. Grain refinement

with increasing HA content also aligns well with the surface hardness values. Literature has shown that grain refinement increases the mechanical properties of a material. Properties such as strength, fracture toughness, corrosion resistance, and the ability to resist deformation, i.e., hardness [27–30]. This is due to the increase in 'barriers' such as grain boundaries, refraining, or suppressing dislocation motion upon deformation, with the addition of 2wt.% HA to Ti64, the surface hardness increased by 57% from $377 \pm 21HV_{0.2}$ to $592 \pm 25HV_{0.2}$. Surface hardness for the 3HA composition increased to $645 \pm 33HV_{0.2}$, which increases 71% compared to the Ti64 control. In the present study, the presence of HA correlated to an increase in hardness, but previous work has reported that in a CoCrMo matrix, this is not the case [31]; although, wear resistance has shown improvement.

4.2 Tribological and Bio-tribological testing: An array of testing was carried out where the media and the counter wear material used were varied while maintaining the same normal load, travel path, and total slide distance constant. Testing with DMEM and a ZrO_2 counter wear ball was done to emulate an *in vitro* environment. Observed from the tribological data was a reduction in final contact pressure variation when testing in DMEM with the ZrO_2 counter wear ball, but increased variation amongst the compositions when testing in DI water with a WC counter wear ball. The observed contact pressures of all the testing still fell within the range of reported hip joint contact pressure distributions within a hip lateral center-edge (CE) angle range of 14 – 30° at an abductor angle of 0 – 40° or from and abductor angle of 15 – 40° at a CE angle of 8° [32]. Across all testing conditions, the counter wear balls tested with the 2HA composition exhibited the least amount of volume loss, but when coupling the 2HA composition with the ZrO_2 counter wear ball in DMEM, cohesive failure of the Ti-based matrix was observed by an

increase in Ti material transfer; this adhesive wear was most predominant with the Ti64 control composition when testing on ZrO_2, and HCS counter wear balls. Ti is a passive metal that has been reported to display low resistance to plastic shear, exhibiting both cohesive and adhesive dynamic failure mechanisms, in some cases [33]; this would explain the observed grooving, plowing, and plastically sheared wear scar surface observed amongst the different testing conditions for Ti64 and most predominantly observed on the ZrO_2 counter wear ball in DMEM. Additionally, Ti's adiabatic shear characteristic induces a loss in load carrying capacity and can help explain COF's observed reduction across the 3 testing conditions. Additionally, the Ti64 control exhibited lower wear rates in a non-corrosive environment than the 2HA and 3HA compositions tested in DI water. The passive nature of Ti can explain this, it would appear that it acted upon cohesive failure and adhesion to the counter wear ball. The Ti acted as its own solid lubricant, but not ideal as there was observable excess material removal and transfer to the counter wear ball. Although, once the Ti64 composition was tested in DMEM on a ZrO_2 counter wear ball, its calculated wear rate and compound wear was higher than the 2HA and 3HA compositions – inferior tribological behavior in an *in vitro* environment. With the addition HA, particularly for 3HA, COF was observed to increase even when hardness increased; this phenomenon is most notably due to third body wear as the HA is harder than the surrounding Ti matrix. Although this may be the case, aggressive wear modes appear to have been suppressed, as the wear tracks were smoother and shallower. Similar third body abrasive wear has been reported in previous work [34]. Thus, explaining the increased wear rate in both DI water testing conditions. When testing with a ZrO_2 counter wear ball, it appears that the lubricating nature associated with DMEM suppressed the minimal third body wear and allowed for reduced wear rate, determined from compound wear, for both 2HA and 3HA. Thus, a smooth wear track and

minimal Ti transfer to the counter wear ball were validated by optical images of the ZrO2 counter wear ball and Ti elemental mapping of the HCS counter wear ball. Additionally, the HA presence at the wear surface appeared to be constant throughout testing and allowed for a tribofilm formation, as observed by EDS analysis of the wear scar. Thus, these results give insight into the importance of the coupling of adequate materials and the importance of the media interaction with the said materials, such as how the body has done well with the tribological system comprising bone, cartilage, and synovial fluid.

To further analyze the contact surface under dynamic conditions, CR was acquired during tribological testing. The HA composites exhibited an increase in CR consistently for the entirety of DI water testing when testing with both a WC and an HCS counter wear ball. All compositions initially exhibited higher CR values due to the naturally forming passivation layer on the surface of Ti or TiO_2 presence, but it appears that after 50m, the layer was removed, resulting in a drop in the CR values, exposure to the pure metal and most apparent for Ti64. Composites 2HA and 3HA both deviate to greater CR values when compared to Ti64 and remain so during testing, indicative of the formation of the previously HA-based tribofilm. The 2-wire circuit setup for CR applies a constant current between the two terminals, and the voltage drop is measured; in this manner, the resistance is determined. Therefore, CR values are directly correlated to the physical contact between the conductive counter wear ball and the sample being tested. An increase in CR values is indicative of a passive non-conductive or partially conductive layer between the counter wear ball and the sample surface. When testing in DI water with a WC counter wear ball, observed was a significant increase in CR also correlated to a reduction in wear rate. The 2HA composition displayed no significant reduction in wear rate, but CR was considerably steady around ~40Ω for the entirety of testing. Thus, both compositions displayed

the development of the HA-based tribofilm at this instance on the surface when testing against the WC and HCS wear balls. HA was observed at the grain boundaries of 2HA and 3HA and has been previously reported to smear and develop a film on the articulating surface [31]. Wear track surface elemental mapping of 3HA composition revealed a homogenous presence of phosphorous or HA presence on the surface with increased localized presence, most notably due to mechanical adhered particles to the surface. Thereby validating the observed increase in 3HA's CR values. Additionally, when CR was observed to increase for the 3HA composition, its wear rate reduced; this inverse relationship is complementary. If a tribofilm forms, it is expected that the CR would increase and the wear rate decreases. Comparable results have been reported with hypothesized tribofilm formation [26], but minimal to no literature has supported tribofilm's development by *in situ* CR data. In general, surface electron micrographs of the wear scar explicitly displayed the benefits of the *in situ* formed HA-based tribofilm. In **Fig. 5**, the suppression and reduction of grooves, plowing, plastic deformation, and Ti transfer are shown to the worn ball with HA's addition.

In vivo study: Apart from characterizing the produced compositions by mechanical means, an *in vivo* study was conducted to give insight into each composition's biological response. In the present study, 5-week harvested femurs were used to identify early-stage osseointegration. As mentioned, although 5-week and 12-week time points were used to analyze the interfacial strength between the implants and the surrounding host tissue, all 12-week samples fractured during push-out testing, and therefore the data could not be tabulated. The 5-week data displayed a noticeable increase in shear modulus for HA containing samples. The push-out results correlate well with the histological images displayed in **Fig. 9** & **Fig. 10**.

Specimen Ti64 revealed the red/orange presence – indicative of the osteoid presence, but the 2HA specimen displayed a more significant osteoid presence. The 3HA specimen displayed the most significant amount of osteoid formation and the highest shear modulus. Clear or white regions represent trabecular bone that doesn't stain with the modified Masson-Goldner trichrome method, staining of these regions would require a histochemical analysis such as Hematoxylin & Eosin (H&E) and von Willebrand Factor (vWF). However, thin sectioning would be required and is very challenging when a metallic implant is present. Our previous work with tricalcium phosphate (TCP) scaffolds and H&E analysis focused on these areas has shown that these regions are, in fact, of trabecular bone [35]. While comparing, published shear modulus and shear strength values can become complicated due to different studies' varying species. Variations among the same species arise based on gender, age, activity, and even eating habits. Nevertheless, in an attempt to establish a frame of reference, some published values are reported in **Table 3** to allow for a 'relative' comparison with the present study's shear modulus values. Across the reported work, it would seem that HA coating or designed porosity are standard for improving the bond between the host tissue and the implant. This is due to the induced positive tissue response, even when differing processing techniques are used for HA.

It has been shown that the presence of HA on the surface of an implant increases bone formation. The proposed mechanism is that an HA-based coating on an implant will undergo dissolution, producing Ca^{2+} and PO_4^{3-} ions and dissociate into the microenvironment between the implant and host tissue [36]. Reprecipitation occurs and produces a carbonated apatite on the surface of the implant [37]. Serum proteins and cellular integrin receptors bind with the precipitates and allow the bone formation to occur at both the host tissue and implant surface [38,39]; thus, allowing for the implant surface to become bioactive. Bone growth occurs at both

the implant surface and the host tissue surface, increasing the rate of bone formation. Between push-out data and histological results, it can be concluded that the addition of HA increased positive tissue response on the implant surface in the present study, resulting in an increase in the osteoid presence and improved tissue integration supported by the increase in shear modulus values.

5.0 Conclusions

In an attempt to simultaneously improve the wear resistance and induced positive tissue response of Ti64 alloy, HA reinforced Ti64 composites were processed via DED-based AM. Hardness testing resulted in an increase of 57% and 71% for 2HA and 3HA compositions when compared to the Ti64 control, respectively. The microstructural and elemental analysis concluded the presence of HA at β-Ti grain boundaries. The CR and surface mapping validated HA-based tribofilm's presence. Reduced wear rates were achieved when testing *in vitro* in DMEM with a ceramic counter ball. All tested counter materials resulted in <1% wear ball volume loss. The Sprague Dawley rat *in vivo* study revealed improved tissue response, observed by an increase in shear modulus from push-out testing and increased osteoid presence by histomorphometric analysis. The current study results open up the potential use of Ti64-HA-based composites for patients with compromised bone regeneration ability and areas where articulation may degrade the Ti alloy.

6.0 Conflict of interest

The authors declare no conflict of interest.

7.0 Acknowledgements

Authors acknowledge financial support from the National Science Foundation under grant # CMMI 1934230 (PI - Bandyopadhyay) and grant # 1538851 (PI - Bandyopadhyay). Authors also acknowledge financial support from the National Institute of Arthritis and Musculoskeletal and Skin Diseases of the National Institutes of Health under Award Number R01 AR067306. The content is solely the authors' responsibility and does not necessarily represent the National Institutes of Health's official views.

8.0 Data availability statement

All raw data for this study has been presented in this manuscript.

9.0 References

[1] S. Bose, D. Ke, H. Sahasrabudhe, A. Bandyopadhyay, Additive manufacturing of biomaterials, Prog. Mater. Sci. 93 (2018) 45–111. https://doi.org/10.1016/j.pmatsci.2017.08.003.

[2] A. Bandyopadhyay, A. Shivaram, M. Isik, J. D. Avila, W. S. Dernell, S. Bose, Additively manufactured calcium phosphate reinforced CoCrMo alloy: Bio-tribological and biocompatibility evaluation for load-bearing implants, Addit. Manuf. 28 (2019) 312–324. https://doi.org/10.1016/j.addma.2019.04.020.

[3] H. J. Cooper, Diagnosis and Treatment of Adverse Local Tissue Reactions at the Head-Neck Junction, J. Arthroplasty. 31 (2016) 1381–1384. https://doi.org/10.1016/j.arth.2016.02.082.

[4] D.J. Berry, Introduction: The "New" Disease: Taper Corrosion After Total Hip Arthroplasty—A State-of-the-Art Update, J. Arthroplasty. 33 (2018) 2705–2706. https://doi.org/10.1016/j.arth.2018.07.008.

[5] R. Pourzal, H.J. Lundberg, D.J. Hall, J.J. Jacobs, What Factors Drive Taper Corrosion?, J. Arthroplasty. 33 (2018) 2707–2711. https://doi.org/10.1016/j.arth.2018.03.055.

[6] H. Migaud, S. Putman, G. Kern, R. Isida, J. Girard, N. Ramdane, C.P. Delaunay, Do the Reasons for Ceramic-on-ceramic Revisions Differ From Other Bearings in Total Hip Arthroplasty?, Clin. Orthop. Relat. Res. 474 (2016) 21. https://doi.org/10.1007/s11999-016-4917-x.

[7] W. G. Hamilton, J. P. McAuley, T. J. Blumenfeld, J. P. Lesko, S. E. Himden, D. A. Dennis, Midterm Results of Delta Ceramic-on-Ceramic Total Hip Arthroplasty, J. Arthroplasty. 30 (2015) 110–115. https://doi.org/10.1016/j.arth.2015.02.047.

[8] A. A. Vu, S. F. Robertson, D. Ke, A. Bandyopadhyay, S. Bose, Mechanical and biological properties of ZnO, SiO2, and Ag2O doped plasma-sprayed hydroxyapatite coating for orthopedic and dental applications, Acta Biomater. 92 (2019) 325–335. https://doi.org/10.1016/j.actbio.2019.05.020.

[9] A. L. Paschoal, E. C. Vanâncio, L. De Campos Franceschini Canale, O. L. Da Silva, D. Huerta-Vilca, A. De Jesus Motheo, Metallic biomaterials TiN-coated: Corrosion analysis and biocompatibility, Artif. Organs. 27 (2003) 461–464. https://doi.org/10.1046/j.1525-1594.2003.07241.x.

[10] Y. Zhu, W. Wang, X. Jia, T. Akasaka, S. Liao, F. Watari, Deposition of TiC film on titanium for abrasion-resistant implant material by ion-enhanced triode plasma CVD, Appl. Surf. Sci. 262 (2012) 156–158. https://doi.org/10.1016/j.apsusc.2012.03.152.

[11] D. Nolan, S.W. Huang, V. Leskovsek, S. Braun, Sliding wear of titanium nitride thin films deposited on Ti-6Al-4V alloy by PVD and plasma nitriding processes, Surf. Coatings Technol. 200 (2006) 5698–5705. https://doi.org/10.1016/j.surfcoat.2005.08.110.

[12] B.J. Knapp, F.M. Kimock, R.H. Petrmichl, N.D. Galvin, Ion beam process for deposition of highly abrasion-resistant coatings, U.S. Patent 5,508,368, 1996.

[13] H. C. Man, S. Zhang, F. T. Cheng, X. Guo, In situ formation of a TiN/Ti metal matrix composite gradient coating on NiTi by laser cladding and nitriding, Surf. Coatings Technol. 200 (2006) 4961–4966. https://doi.org/10.1016/j.surfcoat.2005.05.017.

[14] H. Sahasrabudhe, J. Soderlind, A. Bandyopadhyay, Laser processing of in situ TiN/Ti composite coating on titanium, J. Mech. Behav. Biomed. Mater. 53 (2016) 239–249. https://doi.org/10.1016/j.jmbbm.2015.08.013.

[15] A. International, G133 – 05: Standard Test Method for Linearly Reciprocating Ball-on-Flat Sliding Wear, Annu. B. ASTM Stand. 05 (2016) 1–10. https://doi.org/10.1520/G0133-05R10.2.

[16] Wikipedia.com, Circular Segment, Wikipedia. (2018). https://en.wikipedia.org/wiki/Circular_segment (accessed May 11, 2020).

[17] A. M. Parfitt, M. K. Drezner, F. H. Glorieux, J. A. Kanis, H. Malluche, P. J. Meunier, S. M. Ott, R. R. Recker, Bone Histomorphometry : Standardization of Nomenclature, Symbols, and Units, J. Bone Miner. Res. 2 (1987) 595–610.

[18] T. He, C. Cao, Z. Xu, G. Li, H. Cao, X. Liu, C. Zhang, Y. Dong, A comparison of micro-CT and histomorphometry for evaluation of osseointegration of PEO-coated titanium implants in a rat model, Sci. Rep. 7 (2017) 1–11. https://doi.org/10.1038/s41598-017-16465-4.

[19] S. Vandeweghe, P.G. Coelho, C. Vanhove, A. Wennerberg, R. Jimbo, Utilizing micro-computed tomography to evaluate bone structure surrounding dental implants: A comparison with histomorphometry, J. Biomed. Mater. Res. - Part B Appl. Biomater. 101

(2013) 1259–1266. https://doi.org/10.1002/jbm.b.32938.

[20] K. Li, C. Wang, J. Yan, Q. Zhang, B. Dang, Z. Wang, Y. Yao, K. Lin, Z. Guo, L. Bi, Y. Han, Evaluation of the osteogenesis and osseointegration of titanium alloys coated with graphene: an in vivo study, Sci. Rep. 8 (2018) 1–10. https://doi.org/10.1038/s41598-018-19742-y.

[21] J. Sun, Y. Yang, D. Wang, Mechanical properties of a Ti6Al4V porous structure produced by selective laser melting, Mater. Des. 49 (2013) 545–552. https://doi.org/10.1016/j.matdes.2013.01.038.

[22] W.F. Hosford, Physical Metallurgy, Second Edition, Taylor & Francis, 2010.

[23] E. Chikarakara, S. Naher, D. Brabazon, High-speed laser surface modification of Ti-6Al-4V, Surf. Coatings Technol. 206 (2012) 3223–3229. https://doi.org/10.1016/j.surfcoat.2012.01.010.

[24] V. Cain, L. Thijs, J. Van Humbeeck, B. Van Hooreweder, R. Knutsen, Crack propagation and fracture toughness of Ti6Al4V alloy produced by selective laser melting, Addit. Manuf. 5 (2015) 68–76. https://doi.org/10.1016/j.addma.2014.12.006.

[25] A. A. Fomin, I. V. Rodionov, Chemical Composition, Structure, and Properties of the Surface of Titanium VT1-00 and Its Alloy VT16 after Induction Heat Treatment, in Handb. Nanoceramics Nanocomposite Coatings Mater., 2015: pp. 403–424.

[26] A. Bandyopadhyay, S. Dittrick, T. Gualtieri, J. Wu, S. Bose, W.M. Keck, Calcium phosphate–titanium composites for articulating surfaces of load-bearing implants, J. Mech. Behav. Biomed. Mater. 57 (2016) 280–288. https://doi.org/10.1016/j.jmbbm.2015.11.022.

[27] M. Bermingham, S. McDonald, M. Dargusch, D. StJohn, Grain-refinement mechanisms in titanium alloys, J. Mater. Res. 23 (2007) 97–104. https://doi.org/10.1557/JMR.2008.0002.

[28] P.W. Early, S.J. Burns, Improved toughness from prior beta grains in Ti-6A1-4V, Scr. Metall. 11 (1977) 867–869. https://doi.org/10.1016/0036-9748(77)90340-4.

[29] J. Yu, Z.J. Zhao, L.X. Li, Corrosion fatigue resistances of surgical implant stainless steels and titanium alloy, Corros. Sci. 35 (1993) 587–597. https://doi.org/10.1016/0010-938X(93)90193-K.

[30] A. Balyanov, J. Kutnyakova, N.A. Amirkhanova, V. V Stolyarov, R.Z. Valiev, X.Z. Liao, Y.H. Zhao, Y.B. Jiang, H.F. Xu, T.C. Lowe, Y.T. Zhu, Corrosion resistance of ultrafine-grained Ti, Scr. Mater. 51 (2004) 225–229. https://doi.org/10.1016/j.scriptamat.2004.04.011.

[31] H. Sahasrabudhe, S. Bose, A. Bandyopadhyay, Laser processed calcium phosphate reinforced CoCrMo for load-bearing applications: Processing and wear induced damage evaluation, Acta Biomater. 66 (2018) 118–128. https://doi.org/10.1016/j.actbio.2017.11.022.

[32] E. Genda, N. Iwasaki, G. Li, B.A. MacWilliams, P.J. Barrance, E.Y.S. Chao, Normal hip joint contact pressure distribution in single-leg standing-effect of gender and anatomic

parameters, J. Biomech. 34 (2001) 895–905. https://doi.org/10.1016/S0021-9290(01)00041-0.

[33] C. Ran, P. Chen, Dynamic shear deformation and failure of Ti-6Al-4V and Ti-5Al-5Mo-5V-1Cr-1Fe alloys, Materials (Basel). 11 (2018). https://doi.org/10.3390/ma11010076.

[34] H. Mohseni, P. Nandwana, A. Tsoi, R. Banerjee, T.W. Scharf, In situ nitrided titanium alloys: Microstructural evolution during solidification and wear, Acta Mater. 83 (2015) 61–74. https://doi.org/10.1016/j.actamat.2014.09.026.

[35] S. Bose, D. Banerjee, S. Robertson, S. Vahabzadeh, Enhanced In Vivo Bone and Blood Vessel Formation by Iron Oxide and Silica Doped 3D Printed Tricalcium Phosphate Scaffolds, Ann. Biomed. Eng. 46 (2018) 1241–1253. https://doi.org/10.1007/s10439-018-2040-8.

[36] J. Dumbleton, M. T. Manley, Hydroxyapatite-coated prostheses in total hip and knee arthroplasty., J. Bone Joint Surg. Am. 86-A (2004) 2526–2540.

[37] R. Z. LeGeros, Properties of osteoconductive biomaterials: calcium phosphates, Clin. Orthop. Relat. Res. 395 (2002) 81–98.

[38] A. E. Porter, L. W. Hobbs, V. Benezra Rosen, M. Spector, The ultrastructure of the plasma-sprayed hydroxyapatite–bone interface predisposing to bone bonding, Biomaterials. 23 (2002) 725–733. https://ac.els-cdn.com/S0142961201001776/1-s2.0-S0142961201001776-main.pdf?_tid=f8f3309f-18b1-48fc-955a-c8fb3443a5b3&acdnat=1529908623_68b33291ca49895de8785192e7dbe2f8 (accessed June 24, 2018).

[39] K. L. Kilpadi, P. L. Chang, S. L. Bellis, Hydroxylapatite binds more serum proteins, purified integrins, and osteoblast precursor cells than titanium or steel, J. Biomed. Mater. Res. 57 (2001) 258–267. https://doi.org/10.1002/1097-4636(200111)57:2<258::AID-JBM1166>3.0.CO;2-R.

[40] M. Muïler, F.F. Hennig, T. Hothorn, R. Stangl, Bone-implant interface shear modulus and ultimate stress in a transcortical rabbit model of open-pore Ti6Al4V implants, J. Biomech. 39 (2006) 2123–2132. https://doi.org/10.1016/j.jbiomech.2005.05.036.

[41] C. Castellani, R. A. Lindtner, P. Hausbrandt, E. Tschegg, S.E. Stanzl-Tschegg, G. Zanoni, S. Beck, A.-M. Weinberg, Bone-implant interface strength and osseointegration: Biodegradable magnesium alloy versus standard titanium control, Acta Biomater. 7 (2011) 432–440. https://doi.org/10.1016/j.actbio.2010.08.020.

[42] G. Schmidmaier, B. Wildemann, P. Schwabe, R. Stange, J. Hoffmann, N.P. Südkamp, N.P. Haas, M. Raschke, A new electrochemically graded hydroxyapatite coating for osteosynthetic implants promotes implant osteointegration in a rat model, J. Biomed. Mater. Res. 63 (2002) 168–172. https://doi.org/10.1002/jbm.10130.

Tables and Figures

Table 1. LENS™ system builds parameters of the fabricated mechanical testing and *in vivo* samples.

Sample	Laser Power (A)	Powder Feed Rate (g/min)	Hatch/Contour Speed (in/min)
Ti64	35	11	16/14
2HA	34-35		16/13
3HA	34-36	11-12	

Table 2. Experimentally measured wear scar dimensions on the counter wear ball to calculated contact pressure and volume loss.

Wear Ball/Media	Sample	Length (mm)	Width (mm)	Depth (mm)	Wear Scar Area (mm^2)	Final Contact Pressure (MPa)	Ball Volume Loss (mm^3)	Ball Volume Loss (%)
WC/DI	Ti64	1.59	0.59	0.03	2.95	2.38	0.06	0.41
	2HA	1.65	0.26	0.01	1.35	5.20	0.01	0.04
	3HA	1.81	0.74	0.05	4.21	1.66	0.13	0.92
HCS/DI	Ti64	1.38	0.56	0.03	2.42	2.89	0.04	0.30
	2HA	1.52	0.32	0.01	1.54	4.56	0.01	0.06
	3HA	1.60	0.52	0.02	2.61	2.68	0.04	0.28
ZrO2/DMEM	Ti64	1.49	0.74	0.05	3.46	2.02	0.11	0.76
	2HA	0.92	0.64	0.03	1.83	3.82	0.04	0.30
	3HA	0.91	0.73	0.05	2.08	3.36	0.06	0.45

Table 3. Push-out data for interfacial shear modulus between host tissue and implant for harvested samples as well as reported values. 12-week samples for the current study -- all samples experienced a bone fracture.

Source	Animal	Implantation Location	Material	Processing	Surface	Shear Modulus / Shear Strength* (MPa)	Time Point (weeks)
Current Study	Male Sprague-Dawley Rat	Femoral metaphysis	Ti64	Laser Engineered Net Shaping	Ground Surface	17.4 ± 3.3	5
			2HA			24.9 ± 2.4	
			3HA			32.4 ± 4.7	
[40]	Female New Zealand White Rabbit	Peri-implant bone – proximal femur	Ti6Al4V	Laser Pulse Technique	Designed porosity	41.1	12
		Periimplant bone – distal femur				25.8	
[2]	Male Sprague-Dawley Rat	Femoral metaphysis	CoCrMo	Laser Engineered Net Shaping	Ground surface	48.0 ± 2.0	12
			CoCrMo + 2 wt.% HA			92.1 ± 6.7	
[41]	Male Sprague-Dawley Rat	Femoral diaphysis	Mg-alloy	As purchased	Smooth surface	2.43*	4
						6.17*	12
						7.65*	24
			Ti-alloy			1.12*	4
						4.14*	12
						2.14*	24
[42]	Female Sprague-Dawley Rat	Retrograde insertion in the medullary cavity of the femur	Titanium Kirschner	None	Uncoated	8.08 ± 3.4*	8
				HA plasma-sprayed Ti-wire	Coated	27.8 ± 6.7*	

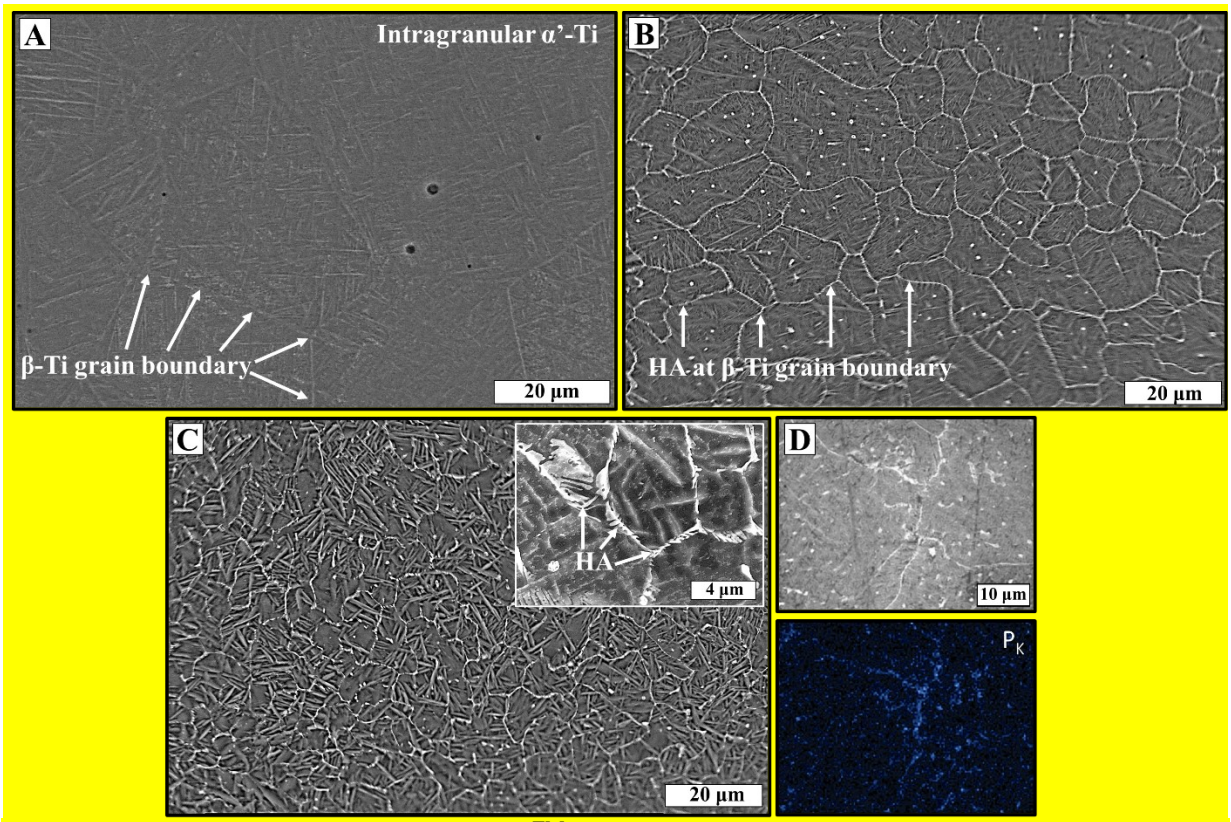

Figure 1: Electron micrographs of LENS^{TM} produced, acid-etched sample surfaces for A) Ti64, B) 2HA, and C) 3HA. Phosphorus elemental mapping was done D) 3HA sample.

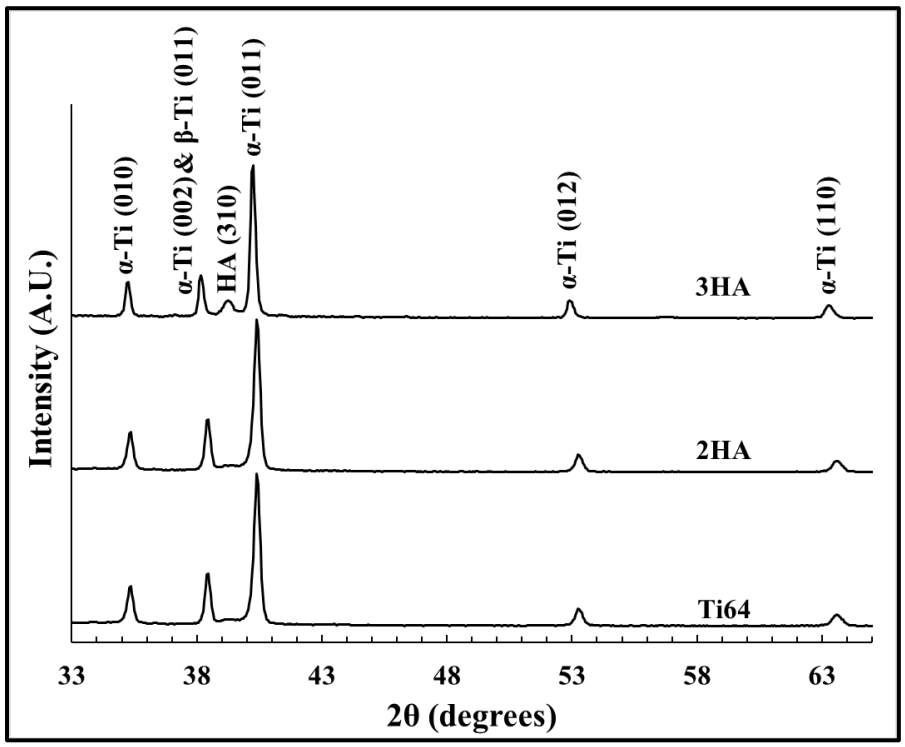

Figure 2: X-ray diffraction spectra of control composition (Ti64), composite 2HA, and 3HA.

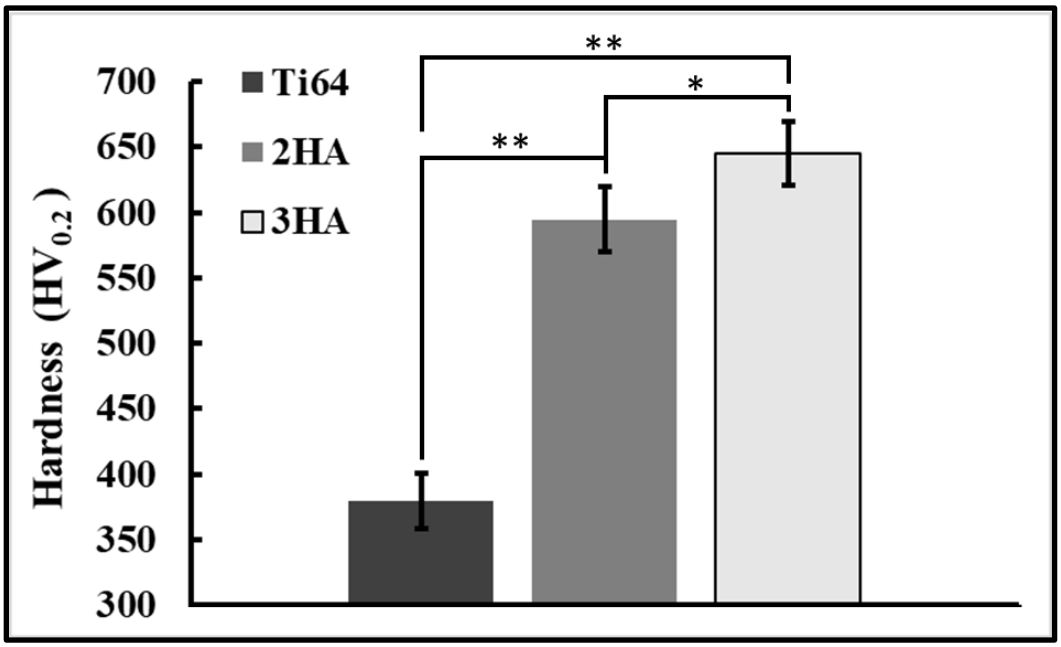

Figure 3. Average Vickers surface hardness for the three DED fabricated samples (n = 9, where (*) correlates to a p-value ≤ 0.0005 and (**) correlates to a p-value 0.0001).

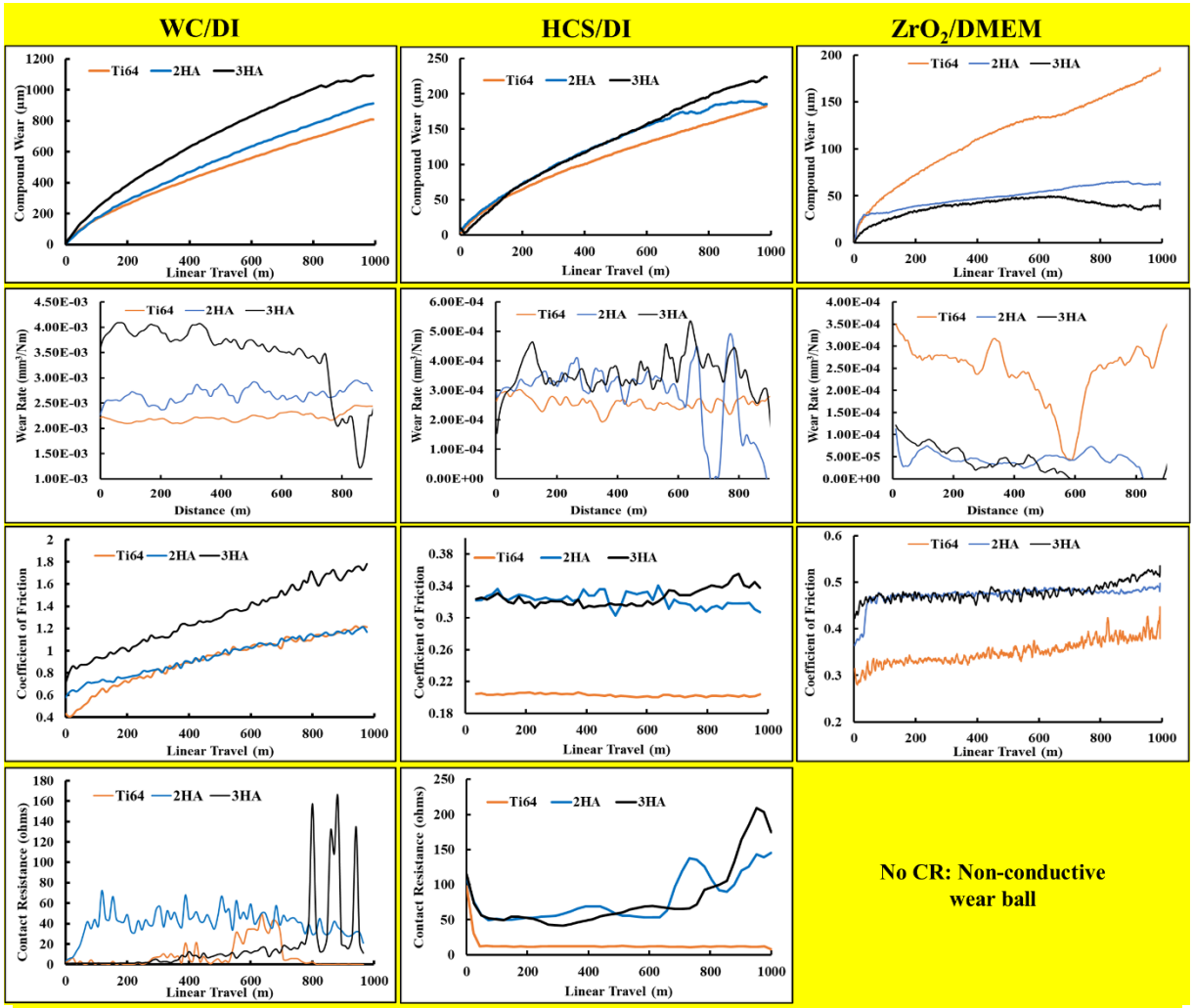

Figure 4: Tribological data for Ti64 control, 2HA, and 3HA of the array of tests in where the counter wear ball was tungsten carbide (WC), hardened chrome steel (HCS), zirconium dioxide (ZrO_2), and media was deionized water (DI) and DMEM. Travel path, load, and total slide distance remained constant.

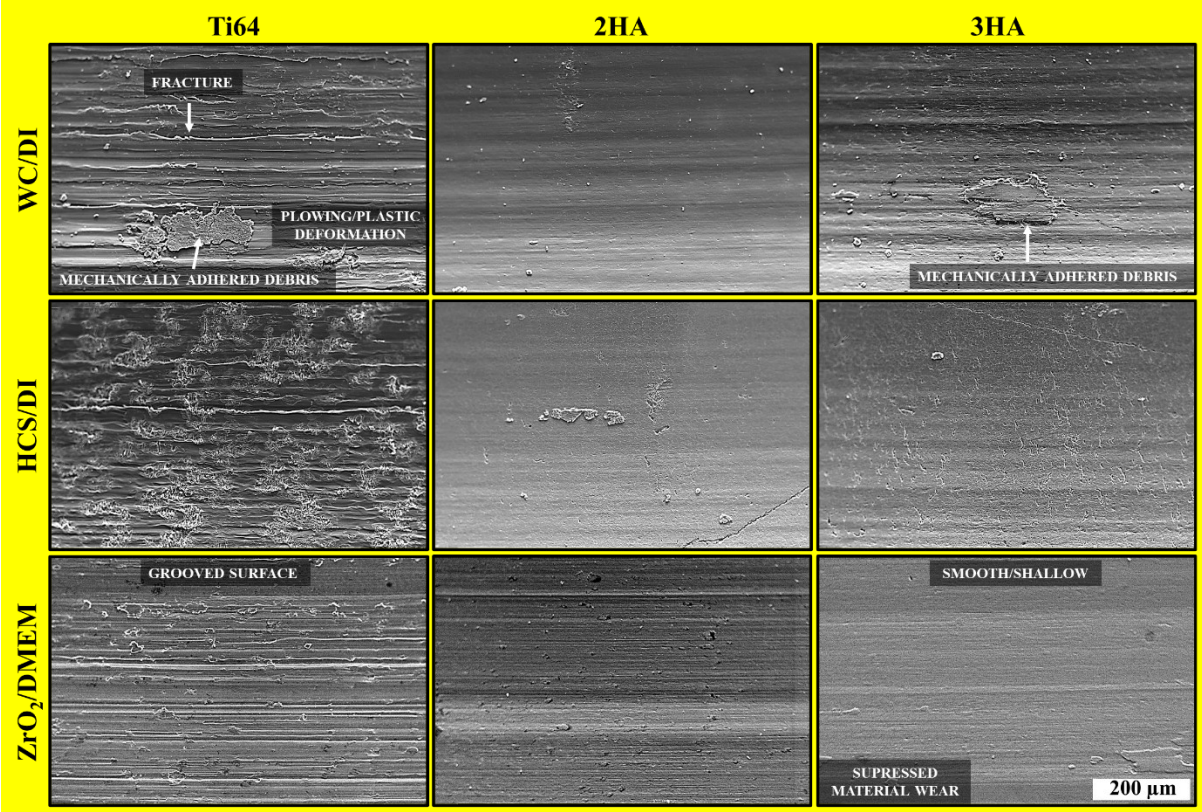

Figure 5: Electron micrographs of the coating wear scar for the varying tribological testing where the counter wear ball and media were varied. Travel path, load, and total slide distance remained constant.

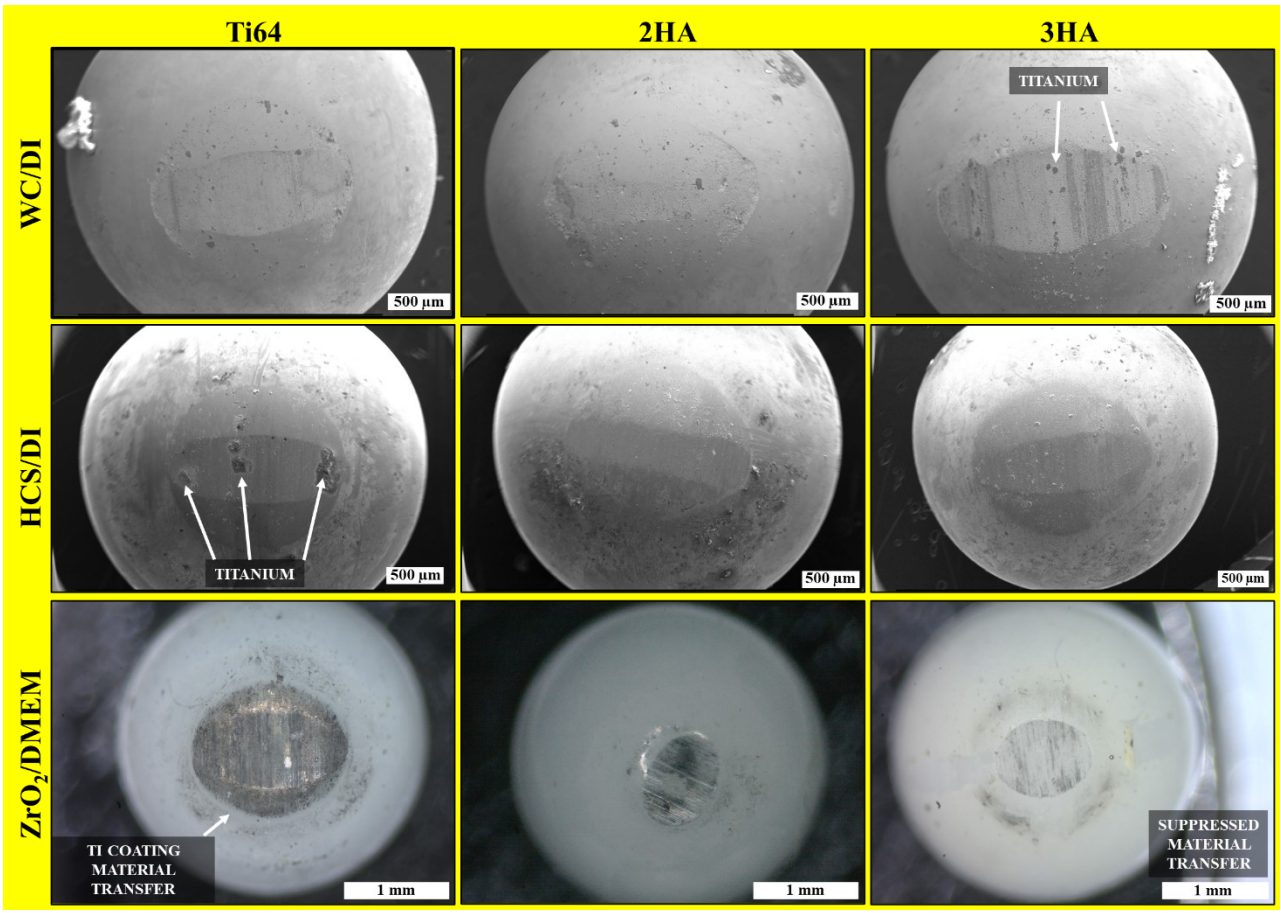

Figure 6: Electron and optical micrographs of the counter wear ball post-tribological testing, where the counter wear ball and media were varied.

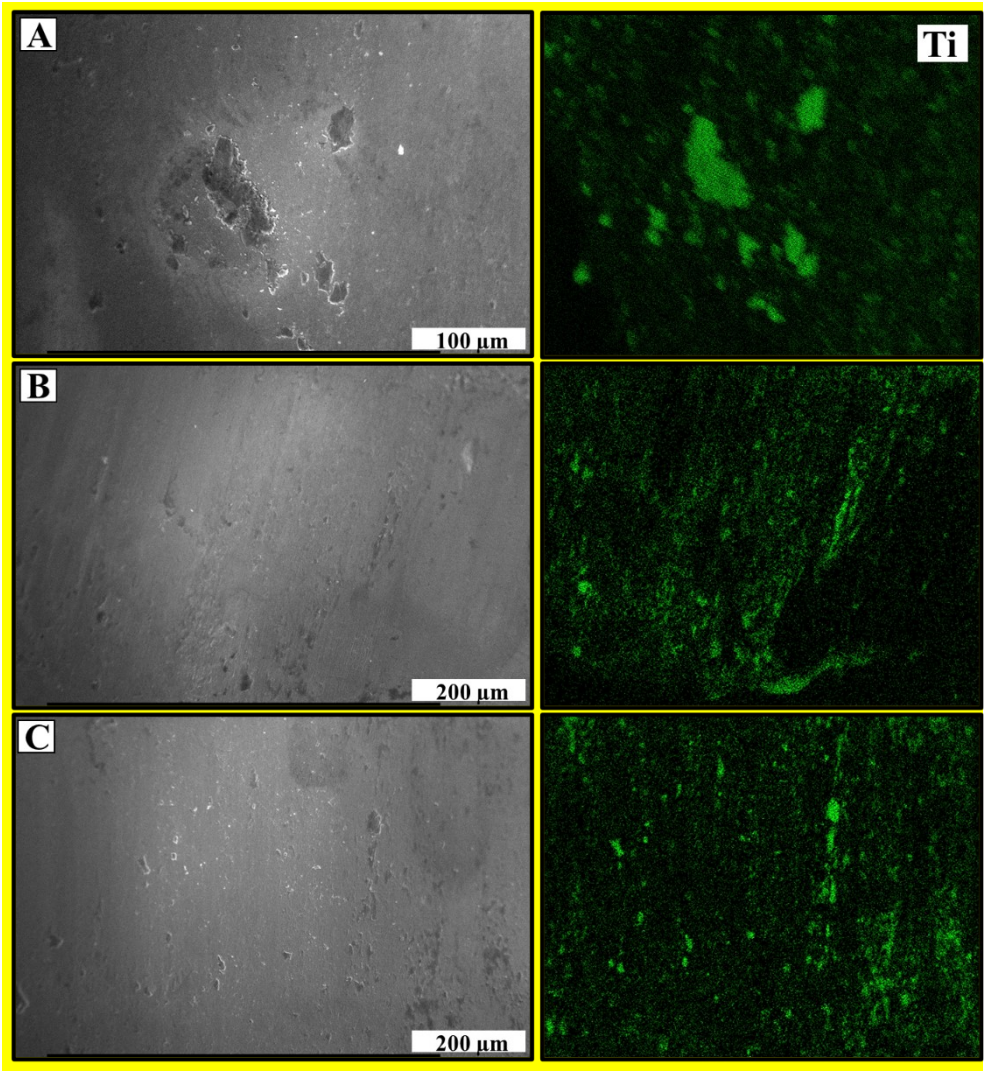

Figure 7: Electron micrographs for A) control Ti64, B) 2HA, C) 3HA and their respective EDS elemental mapping for HCS counter wear ball when tribological tested in DI water.

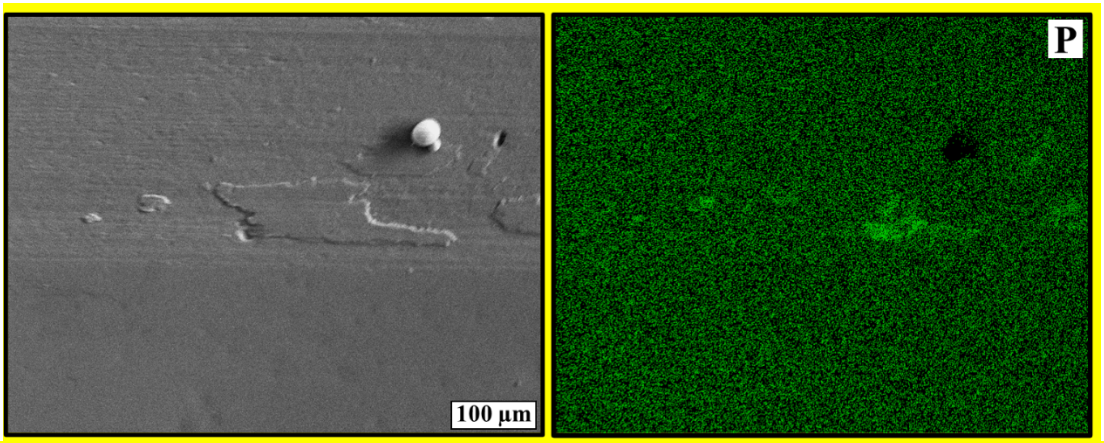

Figure 8: Electron micrograph of the 3HA composition wear track tested in DMEM with a ZrO_2 counter wear ball and its respective phosphorus elemental mapping, displaying a homogeneous surface presence. Al_2O_3 powder particles were intentionally placed on the surface for reassurance of phosphorus mapping and not background signal.

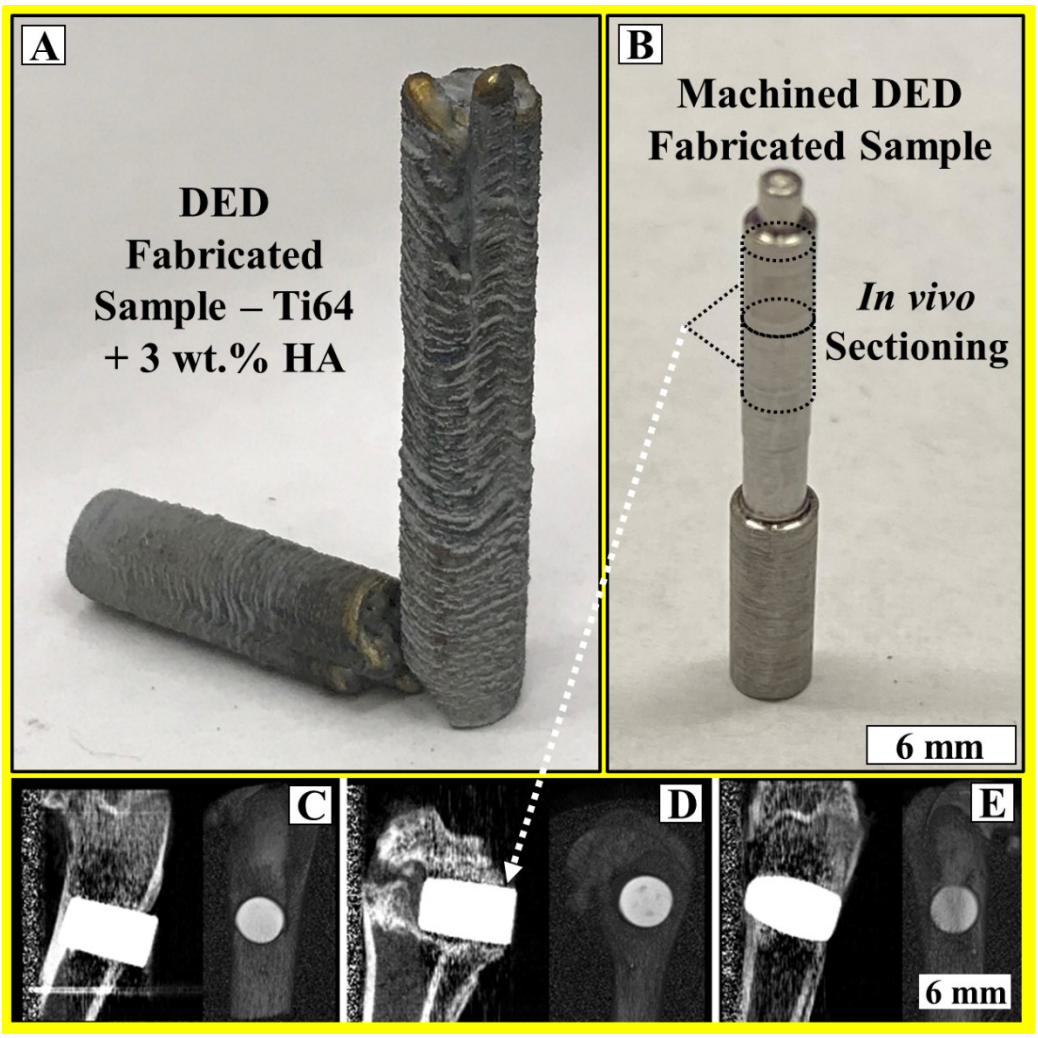

Figure 9: *In vivo* specimens: A) depicts DED fabricated rod and B) the 3mm diameter turned rod. Computed tomography images displaying the 3mm diameter's proper implantation by 5mm long cylindrical specimens into the femur for C) Ti64, d) 2HA, and e) 3HA.

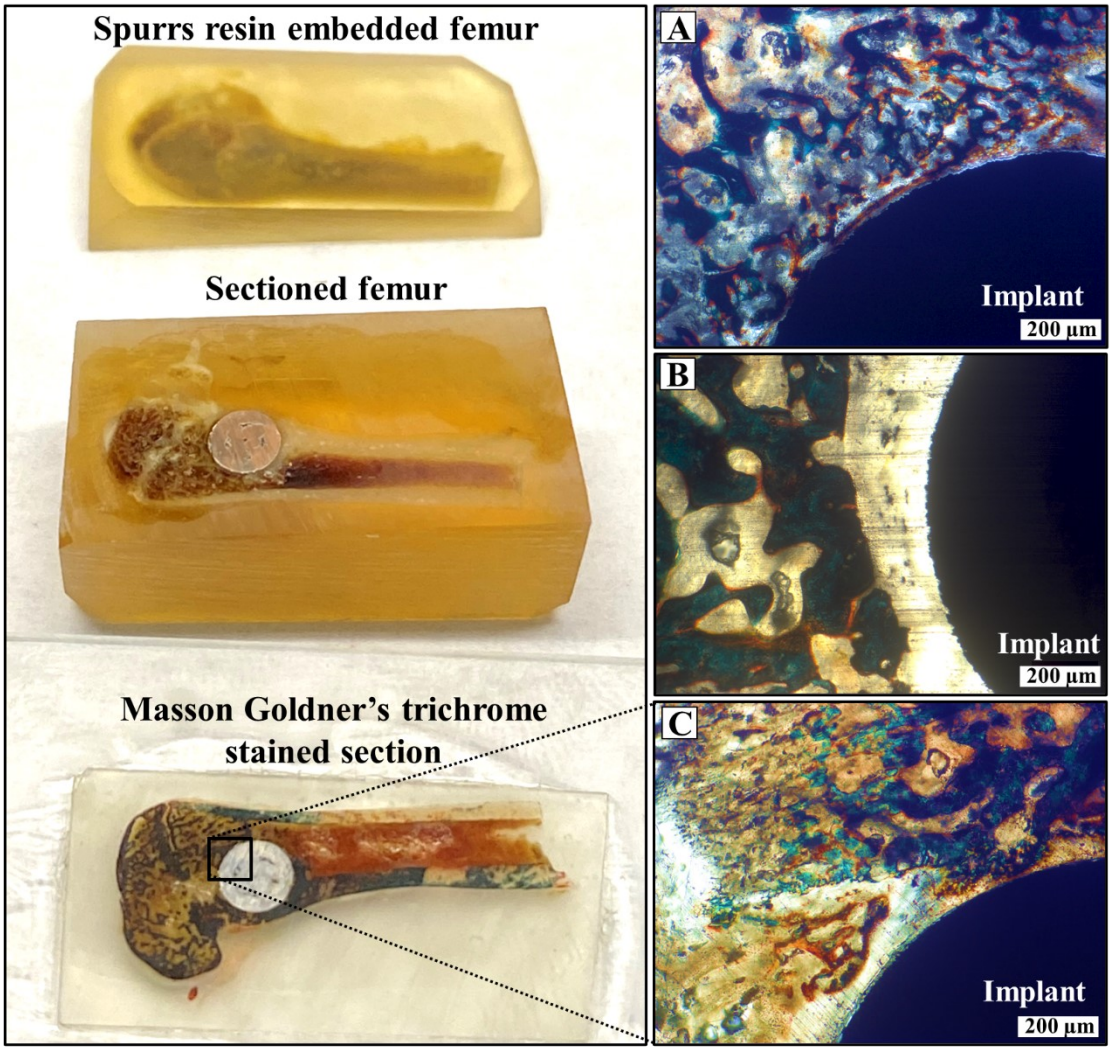

Figure 10: Photomicrographs of harvested, embedded, and Masson Goldner's trichrome stained femurs section for A) Ti64 control, B) 2HA, and C) 3HA at a 5-week time point. Pictured are osteoid tissue (red/orange), mineralized bone (green/blue), and trabecular bone (white).

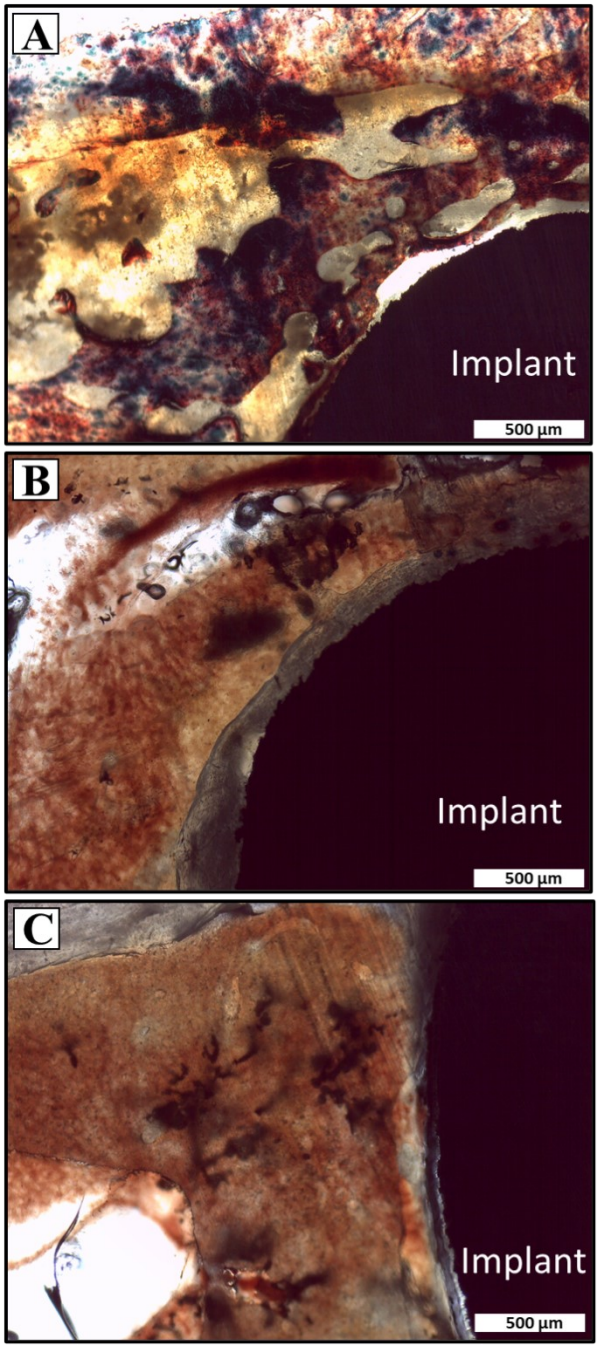

Figure 11: Photomicrographs of harvested and Masson Goldner's trichrome stained femurs section for a) Ti64, b) 2HA, and c) 3HA at a 12-week time point. Pictured are osteoid tissue (red/orange), mineralized bone (green/blue) and extracellular development (white).